MATERIALS CHEMISTRY
FRONTIERS

RESEARCH ARTICLE

View Article Online
View Journal | View Issue

Cite this: *Mater. Chem. Front.*, 2019, **3**, 2673

1T-MoS_2 nanopatch/Ti_3C_2 MXene/TiO_2 nanosheet hybrids for efficient photocatalytic hydrogen evolution†

Yujie Li, Shaorui Yang, Zhangqian Liang, Yanjun Xue, Hongzhi Cui and Jian Tian *

Received 2nd October 2019,
Accepted 23rd October 2019

DOI: 10.1039/c9qm00608g

rsc.li/frontiers-materials

The biggest challenging issue in photocatalytic hydrogen production is to efficiently separate the photoinduced electron–hole pairs, which requires the enrichment of photoinduced electrons on the photocatalyst's surface. Herein, TiO_2 nanosheets (NSs) are *in situ* grown on highly conductive Ti_3C_2 MXene and then 1T-MoS_2 nanopatches are uniformly distributed on the Ti_3C_2/TiO_2 composite through a two-step hydrothermal method. Thus, a unique 2D structure of the Ti_3C_2/TiO_2/1T-MoS_2 composite with double metallic co-catalysts Ti_3C_2 and 1T phase MoS_2 nanopatches is achieved, and the content of 1T phase reaches 84%. The photocatalytic H_2 production rate of the Ti_3C_2/TiO_2/1T-MoS_2 composite with an optimized MoS_2 loading amount (15 wt%) is nearly 132, 11, and 1.5 times higher than that of pure TiO_2 NSs, Ti_3C_2/TiO_2 composites and Ti_3C_2/TiO_2/2H-MoS_2 composites (15 wt%). The 1T-MoS_2 nanopatches on the surface of the Ti_3C_2/TiO_2 composites increase the specific surface area and boost the density of active sites. Besides, the presence of Ti_3C_2 MXene and 1T phase MoS_2 is found to enhance the electronic conductivity, resulting in an increase in efficiency for electron transfer.

1. Introduction

The increasing global demands for energy consumption and consequent environmental pollution have aroused considerable concern to develop clean energy technologies.[1] The generation of hydrogen (H_2) from water using solar energy through semiconductor-based photocatalysis is regarded as a promising strategy for solving global energy problems.[2–5] Among various semiconductor photocatalysts, TiO_2 is currently one of the most extensively used due to its stability against photo and chemical corrosion, low cost and nontoxicity.[6,7] However, the application of TiO_2 is restricted due to the rapid recombination of photo-induced electron–hole pairs, and thus massive endeavors (for instance, surface modification, co-catalyst loading and hetero-junction construction) have been devoted to promoting photo-excited electron and hole separation.[8,9] Among these, the co-catalyst strategies have proven to be one of the most effective ways to improve the photocatalytic hydrogen evolution reaction (HER) performance.[10] Noble metals such as Ag, Pt, Pd and Au are outstanding co-catalysts in photocatalytic H_2 evolution.[11] Nevertheless, the high price and extreme scarcity restrict their application in photocatalytic water splitting.[12] Therefore, seeking an inexpensive and highly active co-catalyst is of paramount significance for achieving photocatalytic H_2 production in the future.[13]

As a new series of two-dimensional (2D) materials, MXenes obtained by the removal of the intermediate element from the MAX phases have attracted tremendous attention because of their excellent electrical conductivity like graphene.[14,15] MAX phases, the precursors of MXenes, have the general formula of $M_{n+1}AX_n$, where M is an early transition metal, A is a group IIIA or IVA element, X is carbon and/or nitrogen, and $n = 1, 2,$ or 3.[16] For example, a 2D material with an accordion-liken structure of layered Ti_3C_2 MXene can be produced by etching the Al layers in HF solution for a certain time from the MAX phase Ti_3AlC_2.[17]

School of Materials Science and Engineering, Shandong University of Science and Technology, Qingdao 266590, China. E-mail: jiantian@sdust.edu.cn

† Electronic supplementary information (ESI) available: XRD patterns of Ti_3AlC_2, Ti_3C_2 MXene and Ti_3C_2/TiO_2 composites; SEM images of bulk 1T phase MoS_2; energy dispersive X-ray spectroscopy (EDS) mapping images of bulk 1T phase MoS_2; TEM images of Ti_3C_2/TiO_2/1T-MoS_2 composites (15 wt% MoS_2); SEM images of Ti_3C_2/TiO_2/1T-MoS_2 composites with different MoS_2 loading amounts of 10 wt%, 25 wt% and 30 wt%; the BET surface area of Ti_3C_2 MXene, Ti_3C_2/TiO_2/1T-MoS_2 composites with different MoS_2 loading amounts (10 wt%, 15 wt%, 25 wt% and 30 wt% MoS_2) and the mixed phase MoS_2; optical photographs of TiO_2 NSs, Ti_3C_2 MXene, Ti_3C_2/TiO_2/1T-MoS_2 composites with different MoS_2 loading amounts (10 wt%, 15 wt%, 25 wt% and 30 wt% MoS_2) and 1T-MoS_2; band gap values of TiO_2; photocatalytic H_2 production of control experiments in the absence of irradiation and photocatalysts; schematic photocatalytic mechanisms for TiO_2 NSs and Ti_3C_2/TiO_2 composites; stability and recyclability of the Ti_3C_2/TiO_2/1T-MoS_2 composites (15 wt% MoS_2); SEM images of Ti_3C_2/TiO_2/1T-MoS_2 composites (15 wt% MoS_2) after 3 cycles; XRD patterns of Ti_3C_2/TiO_2/1T-MoS_2 composites (15 wt% MoS_2) after 3 cycles; SEM images and EDS mapping images of Ti_3C_2/TiO_2/2H-MoS_2 composites (15 wt% MoS_2). See DOI: 10.1039/c9qm00608g

And the presence of hydrophilic functionalities (–OH and –O) on its surface is due to the etching process, enabling it to easily construct strong connections with various semiconductors and water molecules.[4] Thus, due to its high electrical conductivity and unique layer morphology, Ti_3C_2 MXene is a promising co-catalyst candidate to replace Pt for photocatalytic H_2 production.[18]

MoS_2, as a two-dimensional (2D) layered structure, has received a great deal of attention for its potential application as a promising electrocatalyst for H_2 evolution and has been considered as a promising alternative for noble-metal co-catalysts due to its abundance and low cost.[19] Generally, MoS_2 mainly exists in two different polymorphs, including trigonal prismatic semiconducting phase MoS_2 (2H-MoS_2, a bandgap of $\sim$1.8 eV) and octahedral metallic phase MoS_2 (1T-MoS_2).[20] Both theoretical and experimental research have demonstrated that catalytically active sites of 2H-MoS_2 are only located along the edges of the MoS_2 layers, and the inherent poor conductivity character of 2H-MoS_2 restricts the fast electron transfer during the catalytic HER process.[21,22] While 1T-MoS_2 is different from 2H-MoS_2, it possesses dense active sites (both the basal plane and edges) and a much higher conductivity than 2H MoS_2. So 1T-MoS_2 has been applied to photocatalysis as an efficient co-catalyst and an electron acceptor.[23,24]

In this work, we report an innovative 2D heterojunction by taking advantage of the metallic features of Ti_3C_2 MXene and 1T-MoS_2. A two-step procedure is used to design a new type of photocatalyst Ti_3C_2/TiO_2/1T-MoS_2 where Ti_3C_2 MXene and 1T-MoS_2 play important roles as electron acceptors. First, TiO_2 nanosheets (NSs) are *in situ* grown on the surface of Ti_3C_2 MXenes to construct Ti_3C_2/TiO_2 composites by a facile hydrothermal method. Secondly, we intentionally employ the 1T-MoS_2 nanopatches evenly distributed on the surface of Ti_3C_2/TiO_2 composites using a hydrothermal process, in which octahedral MoO_3 is a source of molybdenum and potassium thiocyanate is a source of sulfur. This process subsequently leads to the formation of an efficient photocatalytic system with close contact between the metallic Ti_3C_2 MXene, 1T-MoS_2 nanopatches and TiO_2 NSs. The newly designed Ti_3C_2/TiO_2/1T-MoS_2 composites not only exhibit drastically improved photocatalytic H_2 evolution performance, but also demonstrate much better stability because of the unique 2D–2D–2D structure.

2. Experimental procedure

2.1. Materials

The Ti_3AlC_2 powder was provided by 11 Technology Co., Ltd, Changchun. Hydrochloric acid (HCl), hydrofluoric acid (HF, 40 wt%), sodium tetrafluoroborate ($NaBF_4$), molybdenum oxide (MoO_3) and potassium thiocyanate (KSCN) were purchased from Sinopharm. All chemicals used were of analytical reagent grade.

2.2. Preparation of Ti_3C_2 MXene nanosheets

In a typical synthesis, 0.5 g Ti_3AlC_2 powder was slowly added to 100 mL 40 wt% HF solution. Then the reaction mixture was stirred for 72 h at room temperature. After that, the mixed solution was separated by vacuum filtration, and washed with deionized water to neutral. Finally, Ti_3C_2 MXene nanosheets were dried in a vacuum oven at 50 °C for 12 h.

2.3. Preparation of Ti_3C_2/TiO_2 composites

For the synthesis of Ti_3C_2/TiO_2 composites, 100 mg Ti_3C_2 MXene and 165 mg $NaBF_4$ were added into 15 mL of 1.0 M HCl. After the solution was stirred and ultrasonically treated for 30 min, it was transferred into a 25 mL Teflon-lined stainless-steel autoclave, which was hydrothermally treated at 160 °C for 12 h. After naturally cooling down to room temperature, the reaction solution was collected by vacuum filtration, and the resulting Ti_3C_2/TiO_2 composites were washed with distilled water several times, and dried in a vacuum oven at 60 °C for 12 h.

2.4. Preparation of Ti_3C_2/TiO_2/1T-MoS_2 composites and Ti_3C_2/TiO_2/2H-MoS_2 composites

For the synthesis of Ti_3C_2/TiO_2/1T-MoS_2 composites, 8.1 mg MoO_3 and 23.15 mg KSCN were dissolved in 30 mL deionized water to form a transparent solution. Then, 60 mg Ti_3C_2/TiO_2 composites were added into the above solution and stirred to form the suspension. After the suspension was stirred, it was ultrasonically treated for 60 min. The solution was transferred into a 50 mL Teflon-lined stainless-steel autoclave, which was hydrothermally treated at 200 °C for 18 h. After naturally cooling down to room temperature, the reaction solution was collected by vacuum filtration, and the resulting Ti_3C_2/TiO_2/1T-MoS_2 composites (15 wt% MoS_2) were washed with distilled water several times, and dried in a vacuum oven at 50 °C for 12 h. Similarly, by changing the mass of MoO_3 (5.4 mg, 13.5 mg, and 16.2 mg) and KSCN (15.4 mg, 38.6 mg, 46.3 mg), Ti_3C_2/TiO_2/1T-MoS_2 composites with other MoS_2 loading amounts (10 wt%, 25 wt%, and 30 wt%) were obtained, respectively. Ti_3C_2/TiO_2/2H-MoS_2 composites with different MoS_2 loading amounts (10 wt%, 15 wt%, 25 wt%, and 30 wt%) were prepared by a hydrothermal method.[22]

2.5. Characterization

The phase constituents of the synthesized products were analyzed by X-ray diffraction (XRD, H-12 KURARAY, Japan). The nanostructure and surface characteristics of the products were observed *via* high-resolution scanning electron microscopy (FESEM, FEI Nova NanoSEM 450, USA) with energy-dispersive X-ray spectroscopy (EDS). High-resolution transmission electron microscopy (HRTEM) was carried out using a JEOL JEM 2100F field emission transmission electron microscope. The chemical states of the composite were tested using X-ray photoelectron spectrometry measurements (XPS, Thermo ESCALAB 250XI, USA). The pore size distribution was measured using the Brunauer Emmett Teller (BET) method as-examined on a Micromeritics ASAP 2020 nitrogen adsorption–desorption apparatus. The UV-vis diffuse reflectance spectra (DRS) of the samples were tested on a UV-vis spectrophotometer (Hitachi UV-3101) with an integrating sphere attachment within the 200–800 nm range. The photoluminescence (PL) spectra were acquired at room temperature using a FLS920 fluorescence spectrometer under the ultraviolet excitation of 325 nm.

2.6. Photocatalytic and photoelectrochemical activity test

The photocatalytic reaction was implemented in a Pyrex glass vessel, with a top quartz window suitable for vertical illumination, connected to a gastight circulation system. The stir rate of the vessel is 550 rpm. A 300 W Xe arc lamp (CELHXF300, Beijing China Education Au-light Co., Ltd) with an AM-1.5 filter was used as the light source. The wavelength range of the AM-1.5 filter is from 200 to 1200 nm. The focused intensity of the flask was *ca.* 180 mW cm^{-2}. The experiments were performed in aqueous acetone which dissolved TEOA (15 mL acetone + 5 mL TEOA + 80 mL deionized water), and suspended with 10 mg of catalyst powder following ultrasonic dispersion for 2 min. Then the reaction solution was evacuated several times to remove air and the reaction temperature of the reactant solution was maintained at 25 °C. The amount of generated hydrogen was analyzed by a gas chromatograph (Techcomp GC-7920) equipped with a thermal conductivity detector (TCD). The apparent quantum efficiency (AQE) was measured using the same light source with a CUT420 filter.

The transient photocurrent response and electrochemical impedance spectroscopy (EIS) curves of the samples were measured by using an electrochemical workstation (Shanghai Chenhua CHI660D) under a 300 W Xe arc lamp with an AM-1.5 filter with light on–off switches of 100 s in a three-electrode electrochemical cell in the 0.5 M Na_2SO_4 electrolyte, in which the Pt wire and the Ag/AgCl electrode were used as the counter and reference electrodes, respectively. 2 mg of the as-synthesized samples were mixed with 0.5 mL ethanol and terpilenol. After being sonicated for 5 min, the mixture was dropped onto fluoride-tin oxide (FTO) conductor glass and dried at 50 °C for 6 h to form a working electrode.

3. Results and discussion

A typical synthesis route of the Ti_3C_2/TiO_2/1T-MoS_2 composites is schematically depicted in Scheme 1. First, the Ti_3C_2 MXene nanosheets are synthesized by selectively etching Al layers in Ti_3AlC_2 MAX phase with HF acid.[25] Second, the layered Ti_3C_2 MXene nanosheets providing Ti sources for the growth of TiO_2 NSs across the layered Ti_3C_2 MXene are achieved through the hydrothermal oxidation of Ti_3C_2 with the assistance of HCl and $NaBF_4$. Then, the obtained Ti_3C_2/TiO_2 composites are immersed in a clear solution with MoO_3 and KSCN at 200 °C for 18 h in order to introduce the MoS_2 cocatalyst. The 1T-MoS_2 nanopatches are evenly distributed over the surface of the Ti_3C_2/TiO_2 composites to form ternary Ti_3C_2/TiO_2/1T-MoS_2 composites.

The phase structure and crystallization of the obtained powder samples were characterized by Xray diffraction (XRD), as shown in Fig. 1 and Fig. S1 (ESI†). The XRD patterns of Ti_3AlC_2, Ti_3C_2 and Ti_3C_2/TiO_2 composites are revealed in Fig. S1 (ESI†). The XRD diffraction peaks of Ti_3AlC_2 are similar to the previous literature.[7] After the etching of Ti_3AlC_2 by HF, the most intense (104) diffraction peak in the Ti_3AlC_2 pattern located at 39° completely disappeared and the (002) plane at 9.58° and (004) plane at 19.17° of Ti_3AlC_2 were broadened and shifted toward the lower angle side due to the expansion of the interlayer spacing, which indicates the successful removal of the Al layers and formation of Ti_3C_2 MXene.[26] The growth of TiO_2 NSs across the layered Ti_3C_2 sheets by the hydrothermal oxidation of Ti_3C_2 is evidenced by the emergence of diffraction peaks of anatase TiO_2 (JCPDS No. 21-1272). Fig. 1 shows the XRD patterns of Ti_3C_2/TiO_2/1T-MoS_2 composites with different MoS_2 loading amounts. The diffraction peaks appearing at 8.9°, 18.5°, 27.6° and 60.4° are indexed to the (002), (004), (006) and (110) planes of Ti_3C_2, and the peaks observed at 25.3°, 37.8°, 48.1°, 53.9°, 55.1°, 62.7°, 68.8°, 70.3°, 75.38° and 82.7° are indexed to the (101), (004), (200), (105), (211), (204), (116), (220), (107) and (224) planes of anatase TiO_2 (JCPDS No. 21-1272). No signals assignable to MoS_2 are detectable. This can be explained by the fact that MoS_2 is ultra-thin and is highly dispersed on the Ti_3C_2/TiO_2/1T-MoS_2 composites.

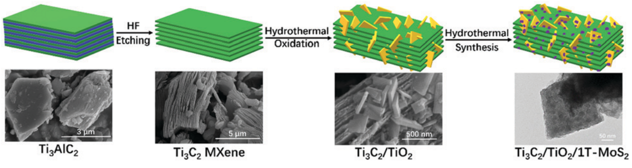

Scheme 1 Schematic illustration of the preparation of Ti_3C_2/TiO_2/1T-MoS_2 composites.

The morphology and structure of the obtained samples are characterized by scanning electron microscopy (SEM), as exhibited in Fig. 2 and Fig. S2 (ESI†). As shown in Fig. 2a, Ti_3C_2 has an accordion-like multilayer structure with a smooth surface, which reveals the typical MXene morphology. Fig. 2b shows that the bulk MoS_2 is about 3–4 microns in size, and is made up of sheets (Fig. S2, ESI†). The EDS mapping of bulk MoS_2 is shown in Fig. S3 (ESI†). After hydrothermal oxidation of Ti_3C_2 MXene, the layered Ti_3C_2 MXene nanosheet acts as the Ti source for the growth of TiO_2 NSs inserted across the layered Ti_3C_2 MXene nanosheet to form Ti_3C_2/TiO_2 composites (Fig. 2c). For the Ti_3C_2/TiO_2/1T-MoS_2 composites (15 wt% MoS_2), the 1T-MoS_2 nanopatches are evenly distributed on the surface of the Ti_3C_2/TiO_2 composites (Fig. 2d), exposing rich active edge sites for H_2 evolution reactions.[20] Furthermore, Ti_3C_2/TiO_2/1T-MoS_2 composites with other different MoS_2 loading amounts (10 wt%, 25 wt%, and 30 wt%) are also obtained, and the corresponding SEM images are shown in Fig. S4 (ESI†).

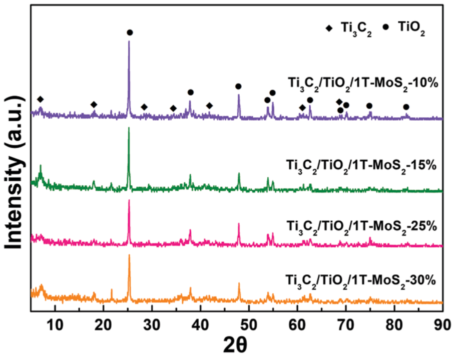

Fig. 1 XRD patterns of Ti_3C_2/TiO_2/1T-MoS_2 composites with different MoS_2 loading amounts (10 wt%, 15 wt%, 25 wt%, and 30 wt%).

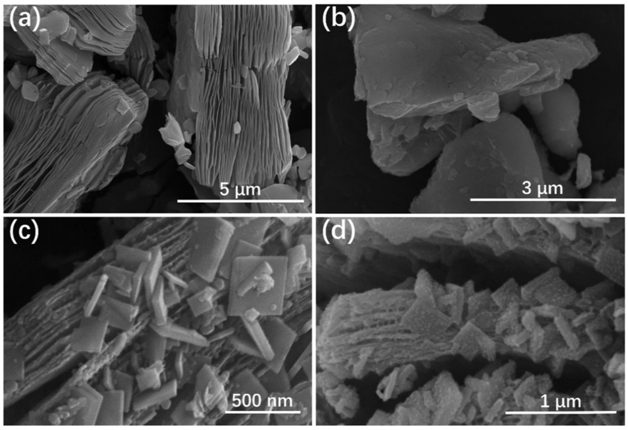

Fig. 2 SEM images of (a) Ti_3C_2 MXene, (b) bulk MoS_2, (c) Ti_3C_2/TiO_2 composites and (d) $Ti_3C_2/TiO_2/1T\text{-}MoS_2$ composites (15 wt% MoS_2).

The morphology and microscopic structure of the $Ti_3C_2/TiO_2/1T\text{-}MoS_2$ composites have been further elucidated by TEM analysis. As shown in Fig. 3a, b and Fig. S5a (ESI†), ultrathin large lamellar Ti_3C_2 MXene sheets, square TiO_2 NSs and small MoS_2 nanopatches can be clearly seen in the $Ti_3C_2/TiO_2/1T\text{-}MoS_2$ composites, which is consistent with the presentation of SEM images in Fig. 2d. The size of the MoS_2 nanopatches in the $Ti_3C_2/TiO_2/1T\text{-}MoS_2$ composites is about 10–20 nm, and the formation of $Ti_3C_2/TiO_2/1T\text{-}MoS_2$ composites could efficiently decrease the particle size of MoS_2 and greatly improve the dispersibility of MoS_2, which further increases the specific surface area of the photocatalyst, facilitates sufficient contact of the catalyst with the reactants, and enhances photocatalytic activity. The HRTEM image, as displayed in Fig. 3c and d, provides more detailed information about the interface between $1T\text{-}MoS_2$ and TiO_2–Ti_3C_2. In detail, the lattices with *d* spaces of 0.98 and 0.26 nm are attributed to the (002) and (0110) planes of Ti_3C_2 MXene, which are the same as the description of the literature.[1,27] The lattice spacing of 0.35 nm is indexed to the (101) plane of anatase TiO_2 (Fig. 3d).[28] Most importantly, the trigonal lattice of the octahedral 1T MoS_2 phase is found, as shown in the inset of Fig. 3d, visualizing and demonstrating the formation of $1T\text{-}MoS_2$ phase,[29] and the number of plies is mostly about 2–5 layers as shown in Fig. 3c and Fig. S5b (ESI†). The EDX elemental mappings of the composite are shown in Fig. 3e, and the Ti, O, Mo and S elements are distributed accordantly within the selected area. The as-fabricated photocatalyst with superior metallic quality of Ti_3C_2 MXene and $1T\text{-}MoS_2$ has faster charge separation and more efficient carrier transfer compared with pure TiO_2 NSs or Ti_3C_2/TiO_2 composites, and hence, the photocatalytic activities are improved.

The X-ray photoelectron spectroscopy (XPS) analysis of $Ti_3C_2/TiO_2/1T\text{-}MoS_2$ composites is investigated to further confirm the chemical composition and states of elements, and the results are shown in Fig. 4. The full-scale XPS pattern of the $Ti_3C_2/TiO_2/1T\text{-}MoS_2$ composites shown in Fig. 4a reveals that Ti, C, O, S, and Mo are the predominant elements, while the F element can be attributed to the F^- ions physically adsorbed on the surface of composites derived from the HF solution. The C 1s XPS spectrum presents two peaks at 284.8 and 282.1 eV, designated to sp^2 carbon (C=C) and C–Ti, respectively,[25] which are attributed to the adventitious elemental carbon and Ti_3C_2 (Fig. 4b). The high-resolution XPS spectrum of Ti 2p is deconvoluted into four peaks as shown in Fig. 4c.[4] The two peaks at binding energies of 459.3 eV (Ti $2p_{3/2}$) and 465.1 eV (Ti $2p_{1/2}$) are attributed to the lattice Ti–O bond in TiO_2,[30] while the other two peaks at binding energies of 455.7 eV (Ti $2p_{3/2}$) and 461.8 eV (Ti $2p_{1/2}$) correspond to the lattice Ti–C bond in Ti_3C_2.[26] The O 1s XPS

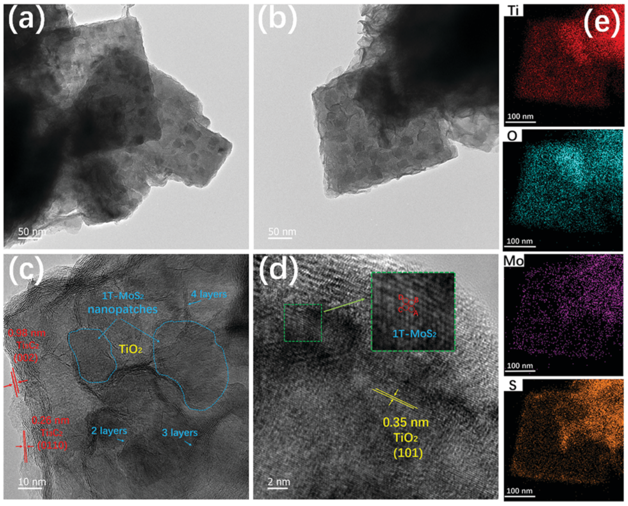

Fig. 3 (a and b) TEM, (c and d) HRTEM and (e) EDX elemental mapping images of $Ti_3C_2/TiO_2/1T\text{-}MoS_2$ composites (15 wt% MoS_2).

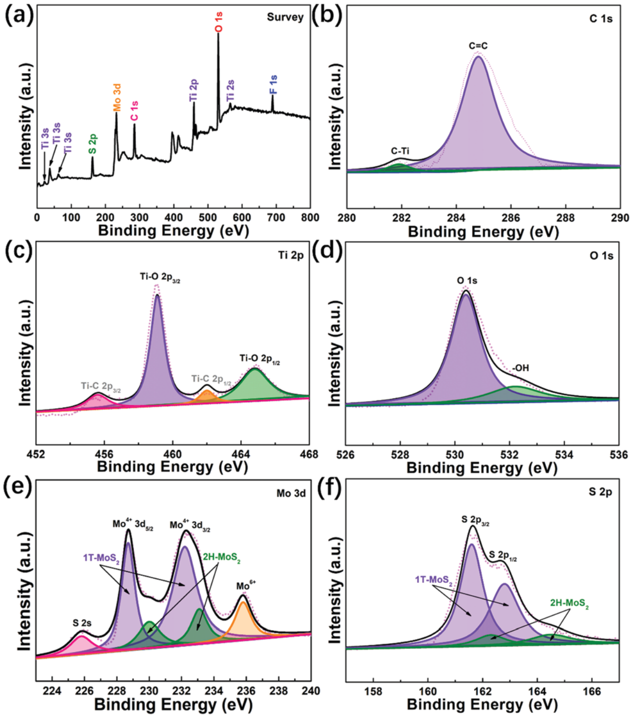

Fig. 4 XPS spectra of (a) fully scanned spectra, (b) C 1s, (c) Ti 2p, (d) O 1s, (e) Mo 3d and (f) S 2p in $Ti_3C_2/TiO_2/1T\text{-}MoS_2$ composites (15 wt% MoS_2).

spectrum (Fig. 4d) exhibits two peaks centered at 530.1 eV and 532.1 eV, corresponding to the bonds of Ti–O–Ti (lattice O) and surface hydroxyl groups,[31] respectively. The Mo 3d and S 2p XPS spectra of $Ti_3C_2/TiO_2/1T\text{-}MoS_2$ composites (Fig. 4e and f) can further verify the identity of 1T MoS_2 and calculate the relative content. In the Mo 3d region, the doublet peaks of 2H phase correlate to Mo $3d_{5/2}$ and Mo $3d_{3/2}$ resonated at around 230.0 eV and 233.0 eV, respectively (Fig. 4e). However, two additional peaks are found to have shifted to lower binding energies at around 228.7 and 232.2 eV, which suggests the presence of metallic 1T phase.[32–34] The peak at 235.9 eV is ascribed to Mo^{6+} arising from MoO_3.[25] Similarly, two peaks located at around 162.3 and 164.0 eV depicted in Fig. 4f correlate strongly to the binding energies of S $2p_{3/2}$ and S $2p_{1/2}$, further clarifying the existence of 2H phase.[35] Meanwhile, additional peaks with a shift to lower binding energies at 161.6 and 162.8 eV have been observed, which once again demonstrates the presence of metallic 1T phase in $Ti_3C_2/TiO_2/1T\text{-}MoS_2$ composites.[36] The high-resolution Mo 3d and S 2p XPS spectra of the composite suggest the predominance of 1T phase (~84% based on the area ratio) over the 2H counterpart (Fig. 4e and f). All of the above results prove the successful generation of 1T-MoS_2 at the surface of Ti_3C_2/TiO_2 composites.

To further analyze the textural properties of the $Ti_3C_2/TiO_2/1T\text{-}MoS_2$ composites, the isotherms and the pore size distributions are studied by N_2 adsorption–desorption measurements (Fig. 5). All the samples possess type IV isotherms with H3 hysteresis loops, suggesting the existence of mesopores.[37,38] The pore-size distribution curve (Fig. 5a–d inset) of the $Ti_3C_2/TiO_2/1T\text{-}MoS_2$ composites with different MoS_2 loading amounts reveals that the size of the dominant mesopores ranges from 3 to 30 nm, and the pore size is mainly distributed about 4 nm. The BET surface area of the as-prepared $Ti_3C_2/TiO_2/1T\text{-}MoS_2$-15%, as shown in Table S1 (ESI†), reveals a higher surface area of 22.138 $m^2\ g^{-1}$, compared with Ti_3C_2 MXene, $Ti_3C_2/TiO_2/1T\text{-}MoS_2$ composites with other MoS_2 loading amounts, and 1T-MoS_2. A larger surface area is favorable in photocatalysis because it can possibly offer more adsorption and active sites, and thus the photocatalytic activity is improved.[39,40]

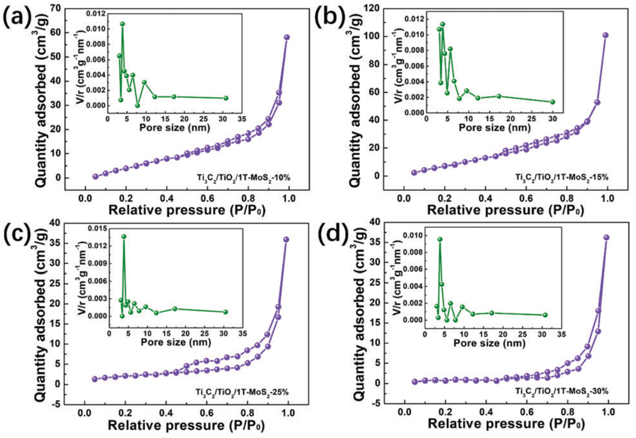

Fig. 5 N_2 adsorption–desorption isotherms and the corresponding pore size distribution curves (inset) of $Ti_3C_2/TiO_2/1T\text{-}MoS_2$ composites with different MoS_2 loading amounts: (a) 10 wt%, (b) 15 wt%, (c) 25 wt%, and (d) 30 wt%.

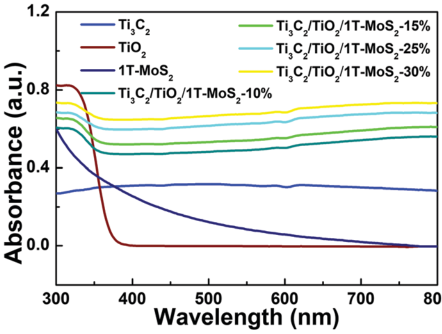

Fig. 6 UV-vis diffuse reflectance spectra of Ti_3C_2 MXene, 1T-MoS_2, TiO_2 NSs and $Ti_3C_2/TiO_2/1T\text{-}MoS_2$ composites (10 wt%, 15 wt%, 25 wt% and 30 wt% MoS_2).

To investigate the optical absorptivity, the UV-vis diffuse refectance spectra (DRS) of the samples were measured. As shown in Fig. 6, TiO_2 NSs (blue curves) possess an obvious absorption in the UV region, and no optical absorption in the visible region, which is consistent with antase TiO_2.[41] Ti_3C_2 MXene (black curves) shows an enhanced visible absorption due to the black color nature (Fig. S6, ESI†). The bulk 1T-MoS_2 is found to exhibit a monotonic increase in the optical absorption as the wavelength decreased from 800 to 400 nm (red curves), indicating the characteristics of a nonplasmonic metallic nanostructure of predominant 1T phases.[42] Compared with TiO_2 NSs, the $Ti_3C_2/TiO_2/1T\text{-}MoS_2$ composites present a significant red shift in the absorption edge and enhanced absorption in the visible-light region, which can be ascribed to the optical absorption of Ti_3C_2 MXene and 1T-MoS_2. Besides, the $Ti_3C_2/TiO_2/1T\text{-}MoS_2$ composites display stronger optical absorption with increasing MoS_2 content. And the derived band gap energy (E_g) from the Kubelka–Munk function (in which $(F(R)h\nu)^2$ is plotted *versus* the photon energy ($h\nu$)) is 3.15 eV for TiO_2 (Fig. S7, ESI†).

The introduction of Ti_3C_2 MXene and 1T-MoS_2 in $Ti_3C_2/TiO_2/1T\text{-}MoS_2$ composites would be expected to influence the separation of photoinduced charge carriers, which could be characterized by steady-state and time-resolved PL spectroscopy (Fig. 7).[43] In general, a lower steady-state PL intensity indicates a longer lifetime and higher separation efficiency of photo-generated electron–hole pairs, leading to higher photocatalytic activity.[44]

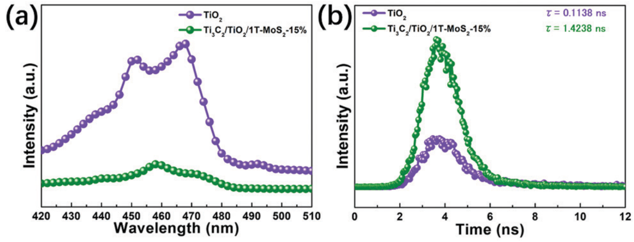

Fig. 7 (a) Steady-state photoluminescence (PL) and (b) time-resolved fluorescence decay spectra of TiO_2 NSs and $Ti_3C_2/TiO_2/1T\text{-}MoS_2$ composites (15 wt% MoS_2), λ_{ex} = 325 nm.

As illustrated in Fig. 7a, it shows that TiO_2 NSs possess a fast recombination of photoinduced charge carriers. When Ti_3C_2 MXene and 1T-MoS_2 are loaded, the PL is drastically quenched (Fig. 7a). Obviously, the recombination of photo-generated e^-–h^+ pairs in TiO_2 can be suppressed by transferring electrons to Ti_3C_2 and 1T-MoS_2 as the electron acceptor. An increased lifetime of charge carriers can be observed by incorporating Ti_3C_2 MXene and 1T-MoS_2 (Fig. 7b), which is in agreement with the steady-state PL measurement results. The intensity-average lifetime (τ) of TiO_2 NSs is 0.1138 ns, which is much lower than that of Ti_3C_2/TiO_2/1T-MoS_2 composites (1.4238 ns). It is believed that the increased lifetime of charge carriers in Ti_3C_2/TiO_2/1T-MoS_2 composites is associated with improved electron transport and charge-separation efficiency.

To gain deep insights into the charge transfer behaviors in the composites, transient photocurrent and electrochemical impedance spectroscopy (EIS) measurements were carried out. The photocurrent responses of the samples were prompted by several on–off cycles of an intermittent 300 W Xe arc lamp with an AM-1.5 filter irradiation in 0.5 M Na_2SO_4 aqueous solution (Fig. 8a and Fig. S8, ESI†). As shown in Fig. S8 (ESI†), pure 1T-MoS_2 and Ti_3C_2 exhibit no photocurrent responses on each illumination, which is consistent with their metallic properties. The TiO_2 NSs and Ti_3C_2/TiO_2/1T-MoS_2 composites exhibit reversible photocurrent responses on each illumination. The photocurrent intensity of the Ti_3C_2/TiO_2/1T-MoS_2 composites is much higher than that of pure TiO_2 NSs, which can be ascribed to the enhanced absorption of visible light as well as improved charge separation and migration efficiency resulting from the addition of 1T-MoS_2 nanopatches inducing the improved light absorption, as well as Ti_3C_2 and metallic 1T-MoS_2 as a co-catalyst more efficiently accepting photo-generated electrons from TiO_2.[27] The EIS measurement is also an effective approach to study the charge transfer process. The Ti_3C_2/TiO_2/1T-MoS_2 composites (Fig. 8b) exhibit a smaller arc radius compared with TiO_2 NSs under light irradiation, suggesting that the Ti_3C_2/TiO_2/1T-MoS_2 composite has smaller charge transfer resistance, ultimately resulting in a high separation and transfer efficiency of photogenerated charge carriers.[45–47]

The photocatalytic performance of Ti_3C_2/TiO_2/1T-MoS_2 composites was evaluated using H_2 evolution under simulated sunlight irradiation in an aqueous acetone solution at room temperature (Fig. 9a and b). Control experiments (Fig. S9, ESI†) indicate that no appreciable H_2 production is detected in the absence of either irradiation or photocatalysts, suggesting that H_2 is produced by a photocatalytic reaction of the photocatalyst.

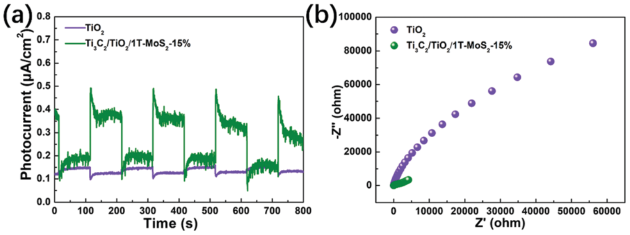

Fig. 8 (a) Transient photocurrent responses and (b) electrochemical impedance spectroscopy (EIS) of TiO_2 NSs and Ti_3C_2/TiO_2/1T-MoS_2 composites (15 wt% MoS_2).

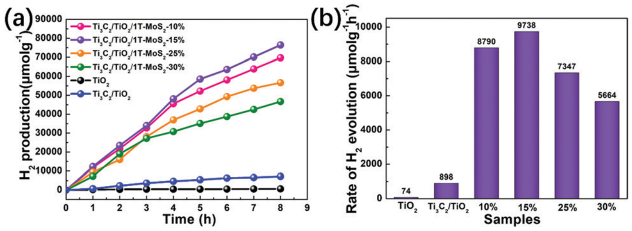

Fig. 9 (a) Photocatalytic H_2 production and (b) rate of photocatalytic H_2 production of different catalysts in aqueous acetone solution with TEOA within 8 h.

As shown in Fig. 9, the pure TiO_2 NSs show a poor photocatalytic H_2 evolution activity (74 μmol g^{-1} h^{-1}), arising from its poor charge separation and transfer capability (Fig. S10a, ESI†). As expected, the photocatalytic H_2 evolution rate of the Ti_3C_2/TiO_2 composites is significantly enhanced (898 μmol g^{-1} h^{-1}), nearly 12 times that of pure TiO_2 NSs. Conductive Ti_3C_2 MXene can serve as a co-catalyst for the efficient capture of photo-generated electrons (Fig. S10b, ESI†), which is crucial to the photocatalytic H_2 production activity of the heterostructure. Notably, after the assembly of 1T-MoS_2 nanopatches, a significantly improved photocatalytic performance is observed, with the highest photocatalytic H_2 evolution rate of 9738 μmol g^{-1} h^{-1} occurring for the Ti_3C_2/TiO_2/1T-MoS_2 composites (15 wt% MoS_2), which is nearly 132 and 11 times higher than that of pure TiO_2 NSs and Ti_3C_2/TiO_2 composites. Moreover, it is worth pointing out that the Ti_3C_2/TiO_2/1T-MoS_2 composite (10 wt% MoS_2), which is composed of a low amount of MoS_2, displays a lower photocatalytic performance compared with the Ti_3C_2/TiO_2/1T-MoS_2 composite (15 wt% MoS_2), because of the relatively poor light absorption (Fig. 6). Furthermore, with the increasing content of MoS_2 from 15 wt% to 30 wt%, a decrease in the photocatalytic activity of Ti_3C_2/TiO_2/1T-MoS_2 composites is discovered. This is because excess black MoS_2 nanopatches absorb photons in the photocatalytic system, probably blocking light from entering into TiO_2, which could be called a "shielding effect".[48]

The stability and durability of a photocatalyst are crucial for practical photocatalytic H_2 production applications. We then further conducted a cycling test of Ti_3C_2/TiO_2/1T-MoS_2 composites (15 wt% MoS_2) for 24 h under the same conditions. As observed in Fig. S11 (ESI†), no obvious decrease in H_2 evolution rate is observed within the three cycles in 24 h. Besides that, the SEM images (Fig. S12, ESI†) and XRD patterns (Fig. S13, ESI†) of the Ti_3C_2/TiO_2/1T-MoS_2 composites after 3 cycles show no obvious difference between those of the fresh sample. This further demonstrates the stability of the Ti_3C_2/TiO_2/1T-MoS_2 composites. We further evaluated the apparent quantum efficiency (AQE) of the samples under a 300 W Xe arc lamp with a CUT420 optical filter. Table S2 (ESI†) shows the comparison of AQE values over TiO_2 NSs, Ti_3C_2/TiO_2 composites and Ti_3C_2/TiO_2/1T-MoS_2 composites with different MoS_2 loading amounts (10 wt%, 15 wt%, 25 wt%, and 30 wt%): 0.0529% (TiO_2 NSs) $<$ 0.644% (Ti_3C_2/TiO_2 composites) $<$ 4.17% (Ti_3C_2/TiO_2/1T-MoS_2-30 wt%) $<$ 5.07% (Ti_3C_2/TiO_2/1T-MoS_2-25 wt%) $<$ 6.24% (Ti_3C_2/TiO_2/1T-MoS_2-10 wt%) $<$ 6.86% (Ti_3C_2/TiO_2/1T-MoS_2-15 wt%).

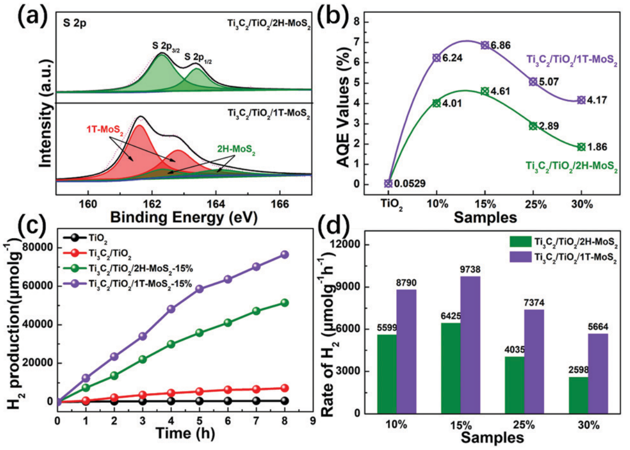

Fig. 10 (a) S 2p XPS spectra in $Ti_3C_2/TiO_2/1T-MoS_2$ composites and $Ti_3C_2/TiO_2/2H-MoS_2$ composites (15 wt% MoS_2). (b) Comparison of the AQE of $Ti_3C_2/TiO_2/1T-MoS_2$ composites and $Ti_3C_2/TiO_2/2H-MoS_2$ composites with different MoS_2 loading amounts. (c) Photocatalytic H_2 production and (d) rate of photocatalytic H_2 production of $Ti_3C_2/TiO_2/1T-MoS_2$ composites and $Ti_3C_2/TiO_2/2H-MoS_2$ composites.

By comparing with the other catalysts (Table S3, ESI†), such as MoS_2/TiO_2 and $1T-MoS_2/TiO_2$, our synthetic $Ti_3C_2/TiO_2/1T-MoS_2$ composites present the best photocatalytic H_2 evolution activity, wherein the presence of Ti_3C_2 MXene and 1T phase MoS_2 shows excellent electronic conductivity, resulting in an increase in efficiency for electron transfer. The results further demonstrate that $Ti_3C_2/TiO_2/1T-MoS_2$ composites can serve as promising photocatalysts for H_2 evolution from water.

To investigate the effect of 1T phase *versus* the 2H counterpart on the photocatalytic activity, the $Ti_3C_2/TiO_2/2H-MoS_2$ composites were prepared and compared. The EDS mapping and TEM images of the $Ti_3C_2/TiO_2/2H-MoS_2$ composites (15 wt% MoS_2) are shown in Fig. S14 and S15 (ESI†). Ultrathin $2H-MoS_2$ NSs are mainly distributed on the surface of TiO_2 NSs and Ti_3C_2 MXene. For the S 2p XPS spectra of $Ti_3C_2/TiO_2/2H-MoS_2$ composites and $Ti_3C_2/TiO_2/1T-MoS_2$ composites (Fig. 10a), the peaks of $1T-MoS_2$ shifted to lower binding energies (about 0.8 eV), as compared with that of $2H-MoS_2$. The AQE and photocatalytic H_2 production activity of the $Ti_3C_2/TiO_2/1T-MoS_2$ composites are also significantly improved (Fig. 10b and c). Specifically, with the same MoS_2 loading of 15%, the H_2 evolution rate of the $Ti_3C_2/TiO_2/1T-MoS_2$ composites reaches 9738 μmol g^{-1} h^{-1} (Fig. 10d), which is 1.5 times higher than that of $Ti_3C_2/TiO_2/2H-MoS_2$ composites (6425 μmol g^{-1} h^{-1}). This suggests that $2H-MoS_2$ can not act well as an electron transport channel and efficient active sites. The photocatalytic H_2 production activity constrained on the edge sites of $2H-MoS_2$ also partly contributes to the decrease of performance. However, $1T-MoS_2$ can serve as a co-catalyst for the efficient capture of photo-generated electrons and active sites for H_2 production.

A possible photocatalytic mechanism for H_2 generation with the $Ti_3C_2/TiO_2/1T-MoS_2$ composites is proposed and illustrated in Scheme 2. Under light irradiation, TiO_2 NSs can be excited to generate electron–hole pairs. Most of the photo-generated electrons in the conduction band (CB) of TiO_2 can immediately transfer to Ti_3C_2 MXene and $1T-MoS_2$ due to the metal characteristic. As a photoelectron receiver, Ti_3C_2 MXene and $1T-MoS_2$ act as active sites for H_2 evolution.[26,49] Meanwhile, the holes in the VB of TiO_2 are consumed by the sacrificial reagents. Thus, the photoinduced electron–hole pairs can effectively be separated and transferred in the presence of double co-catalysts Ti_3C_2 and $1T-MoS_2$.

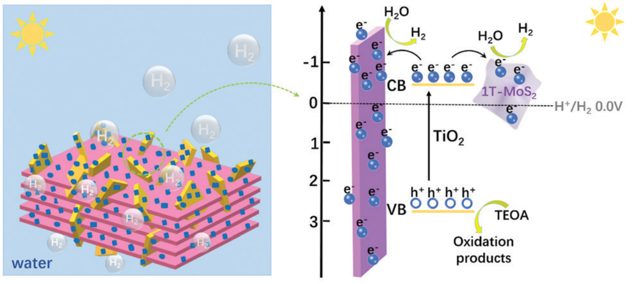

Scheme 2 Schematic photocatalytic mechanism for $Ti_3C_2/TiO_2/1T-MoS_2$ composites.

4. Conclusions

In summary, we have successfully developed an efficient $Ti_3C_2/TiO_2/1T-MoS_2$ composite photocatalyst by a two-step hydrothermal method. The design concept is the *in situ* growth of TiO_2 NSs on the Ti_3C_2 MXene and then 1T phase MoS_2 nanopatches are uniformly distributed on the Ti_3C_2/TiO_2 composites. The obtained $Ti_3C_2/TiO_2/1T-MoS_2$ composite exhibits high photocatalytic H_2 evolution activity with a rate as high as 9738 μmol g^{-1} h^{-1} for the sample with 15 wt% MoS_2 loading, which is nearly 132, 11 and 1.5 times higher than that of pure TiO_2 NSs, Ti_3C_2/TiO_2 composites and $Ti_3C_2/TiO_2/1T-MoS_2$ composites. The high H_2 production activity of $Ti_3C_2/TiO_2/1T-MoS_2$ composites can be attributed to the following: (1) the introduction of MoS_2 nanopatches induces enhanced specific surface area and more active sites on the edges, and the photogenerated electron will react at these active sites; (2) both Ti_3C_2 MXene and $1T-MoS_2$ possess extraordinary conductivity, which greatly enhances the electron transfer ability and thus achieves highly-efficient spatial charge separation.

Conflicts of interest

There are no conflicts to declare.

Acknowledgements

The authors are thankful for funding from the National Natural Science Foundation of China (No. 51872173 and 51772167), the Taishan Scholarship of Young Scholars (no. tsqn201812068), the Taishan Scholarship of Climbing Plan (no. tspd20161006), the Key Research and Development Program of Shandong Province (no. 2018GGX102028) and the Natural Science Foundation of Shandong Province (no. ZR2017JL020).

Notes and references

1 P. Lian, Y. Dong, Z. Wu, S. Zheng, X. Wang, S. Wang, C. Sun, J. Qin, X. Shi and X. Bao, *Nano Energy*, 2017, **40**, 1–8.
2 X. Hao, Z. Jin, H. Yang, G. Lu and Y. Bi, *Appl. Catal., B*, 2017, **210**, 45–56.
3 X. Zhang, Y. Guo, J. Tian, B. Sun, Z. Liang, X. Xu and H. Cui, *Appl. Catal., B*, 2018, **232**, 355–364.
4 J. Ran, G. Gao, F. Li, T. Ma, A. Du and S. Qiao, *Nat. Commun.*, 2017, **8**, 13907.
5 T. Hisatomi, J. Kubota and K. Domen, *Chem. Soc. Rev.*, 2014, **43**, 7520–7535.
6 Z. Liang, X. Bai, P. Hao, Y. Guo, Y. Xue, J. Tian and H. Cui, *Appl. Catal., B*, 2019, **243**, 711–720.
7 Y. Li, X. Deng, J. Tian, Z. Liang and H. Cui, *Appl. Mater. Today*, 2018, **13**, 217–227.
8 X. Yu, X. Han, Z. Zhao, J. Zhang, W. Guo, C. Pan, A. Li, H. Liu and Z. Wang, *Nano Energy*, 2015, **11**, 19–27.
9 J. Low, B. Cheng and J. Yu, *Appl. Surf. Sci.*, 2017, **15**, 658–686.
10 Y. Hou, B. L. Abrams, P. C. K. Vesborg, M. E. Björketun, K. Herbst, L. Bech, A. M. Setti, C. D. Damsgaard, T. Pedersen, O. Hansen, J. Rossmeisl, S. Dahl, J. K. Nørskov and I. Chorkendorff, *Nat. Mater.*, 2011, **10**, 434–438.
11 T. Kamegawa, S. Matsuura, H. Seto and H. Yamashita, *Angew. Chem., Int. Ed.*, 2013, **52**, 916–919.
12 M. J. D. Silva, R. R. Teixeira and D. M. Carari, *J. Organomet. Chem.*, 2009, **694**, 3254–3261.
13 M. Yang, Y. Dong, S. Fei, H. Ke and H. Cheng, *Int. J. Hydrogen Energy*, 2014, **39**, 18976–18983.
14 M. Naguib, O. Mashtalir and J. Carle, *ACS Nano*, 2012, **6**, 1322–1331.
15 M. Naguib, M. Kurtoglu and V. Presser, *Adv. Mater.*, 2011, **23**, 4248–4253.
16 J. C. Lei, X. Zhang and Z. Zhou, *Front. Phys.*, 2015, **10**, 276–286.
17 M. Naguib, V. N. Mochalin, M. W. Barsoum and Y. Gogotsi, *Adv. Mater.*, 2014, **26**, 992–1005.
18 J. Luo, W. Zhang, H. Yuan, C. Jin, L. Zhang, H. Hui, L. Chu, X. Yang, J. Zhang and Y. Gan, *ACS Nano*, 2017, **11**, 2459–2469.
19 K. Chang, M. Li, T. Wang, S. X. Ouyang, P. Li, L. Q. Liu and J. H. Ye, *Adv. Energy Mater.*, 2015, **5**, 1402279.
20 D. Wang, B. Su, Y. Jiang, L. Li, Z. Wu and F. Liu, *Chem. Eng. J.*, 2017, **330**, 102–108.
21 J. F. Xie, H. Zhang, S. Li, R. X. Wang, X. Sun, M. Zhou, J. F. Zhou, X. W. Lou and Y. Xie, *Adv. Mater.*, 2013, **25**, 5807.
22 D. Voiry, M. Salehi, R. Silva, T. Fujita, M. W. Chen, T. Asefa, V. B. Shenoy, G. Eda and M. Chhowalla, *Nano Lett.*, 2013, **13**, 6222.
23 X. Zhang, Z. Lai, C. Tan and H. Zhang, *Angew. Chem., Int. Ed.*, 2016, **55**, 8816–8838.
24 Y. Liu, Y. Li, F. Peng, Y. Lin, S. Yang, S. Zhang, H. Wang, Y. Cao and H. Yu, *Appl. Catal., B*, 2019, **241**, 236–245.
25 Y. Dong, Z. S. Wu, S. Zheng, X. Wang, J. Qin, S. Wang, X. Shi and X. Bao, *ACS Nano*, 2017, **11**, 4792–4800.
26 M. Naguib, M. Kurtoglu, V. Presser, J. Lu, J. Niu, H. Min, L. Hultman, Y. Gogotsi and M. W. Barsoum, *Adv. Mater.*, 2011, **23**, 4207.
27 Z. Zeng, Y. Yan, J. Chen, P. Zan, Q. Tian and P. Chen, *Adv. Funct. Mater.*, 2018, **29**, 1806500.
28 J. Tian, X. Hu, N. Wei, Y. Zhou, X. Xu, H. Cui and H. Liu, *Sol. Energy Mater. Sol. Cells*, 2016, **151**, 7–13.
29 J. W. Shi, Y. Zou, D. Ma, Z. Fan, L. Cheng, D. Sun, Z. Wang, C. Niu and L. Wang, *Nanoscale*, 2018, **10**, 9292.
30 Y. Li, T. Li, J. Tian, X. Wang and H. Cui, *Part. Part. Syst. Charact.*, 2017, **34**, 1700127.
31 X. Hu, S. Lu, J. Tian, N. Wei, X. Song, X. Wang and H. Cui, *Appl. Catal., B*, 2019, **241**, 329–337.
32 C. Peng, P. Wei, X. Y. Li, Y. P. Liu, Y. H. Cao, H. J. Wang, H. Yu and F. Peng, *Nano Energy*, 2018, **53**, 97–107.
33 M. A. Lukowski, A. S. Daniel, F. Meng, A. Forticaux, L. Li and S. Jin, *J. Am. Chem. Soc.*, 2013, **135**, 10274–10277.
34 Y. Li, Qi. Wang, H. Wang, J. Tian and H. Cui, *J. Colloid Interface Sci.*, 2019, **537**, 206–214.
35 H. Liu, T. Lv, C. Zhu, X. Su and Z. Zhu, *J. Mol. Catal. A: Chem.*, 2015, **396**, 136–142.
36 J. M. Ting and T. X. Nguyen, *Chem. – Eur. J.*, 2017, **23**, 17348.
37 F. Yang, Z. Ning and H. Liu, *Fuel*, 2014, **115**, 378–384.
38 K. S. W. Sing, *Pure Appl. Chem.*, 1985, **57**, 603–619.
39 Y. Cui, G. Zhang, Z. Lin and X. Wang, *Appl. Catal., B*, 2016, **181**, 413–419.
40 Q. Liang, Z. Li, X. Yu, Z. H. Huang, F. Kang and Q. H. Yang, *Adv. Mater.*, 2015, **27**, 4634–4639.
41 Z. Zhao, J. Tian, Y. Sang, A. Cabot and H. Liu, *Adv. Mater.*, 2015, **27**, 2557–2582.
42 K. Chang, X. Hai, H. Pang, H. Zhang, L. Shi, G. Liu, H. Liu, G. Zhao, M. Li and J. Ye, *Adv. Mater.*, 2016, **28**, 10033–10041.
43 P. Qiu, C. Xu, H. Chen, F. Jiang, X. Wang, R. Lu and X. Zhang, *Appl. Catal., B*, 2017, **206**, 319–327.
44 M. Schvartzman, V. Sidorov, D. Ritter and Y. Paz, *Semicond. Sci. Technol.*, 2001, **16**, L68–L71.
45 G. Zhang, M. Zhang, X. Ye, X. Qiu, S. Lin and X. Wang, *Adv. Mater.*, 2014, **26**, 805–809.
46 Y. Z. Hong, Z. Y. Fang, B. X. Yin, B. F. Luo, Y. Zhao, W. D. Shi and C. S. Li, *Int. J. Hydrogen Energy*, 2017, **42**, 6738–6745.
47 Y. Liu, W. Wang, Y. W. Wang and X. S. Peng, *Nano Energy*, 2014, **7**, 25–32.
48 H. E. Kim, J. Lee, H. Lee and C. Lee, *Appl. Catal., B*, 2012, **116**, 219–224.
49 A. Manikandan, P. R. Ilango, C. W. Chen, Y. C. Wang, Y. C. Shih, L. Lee, Z. M. Wang, H. Ko and Y. L. Chueh, *J. Mater. Chem. A*, 2018, **6**, 15320.